

Active topoelectrical circuits

Tejas Kotwal,^{1,2} Henrik Ronellenfitsch,² Fischer Moseley,³ Alexander Stegmaier,⁴ Ronny Thomale,⁴ and Jörn Dunkel²

¹*Department of Mathematics, Indian Institute of Technology Bombay, Mumbai 400076, India*

²*Department of Mathematics, Massachusetts Institute of Technology,*

77 Massachusetts Avenue, Cambridge, MA 02139, U.S.A.

³*Department of Physics, Massachusetts Institute of Technology,*

77 Massachusetts Avenue, Cambridge, MA 02139, U.S.A.

⁴*Institut für Theoretische Physik und Astrophysik,*

Universität Würzburg, D-97074 Würzburg, Germany

(Dated: December 4, 2021)

The transfer of topological concepts from the quantum world to classical mechanical and electronic systems has opened fundamentally new approaches to protected information transmission and wave guidance. A particularly promising technology are recently discovered topoelectrical circuits that achieve robust electric signal transduction by mimicking edge currents in quantum Hall systems. In parallel, modern active matter research has shown how autonomous units driven by internal energy reservoirs can spontaneously self-organize into collective coherent dynamics. Here, we unify key ideas from these two previously disparate fields to develop design principles for active topoelectrical circuits (ATCs) that can self-excite topologically protected global signal patterns. Building on a generic nonlinear oscillator representation, we demonstrate both theoretically and experimentally the emergence of self-organized protected edge states in ATCs. The good agreement between theory, simulations and experiment implies that ATCs can be realized in many different ways. Beyond topological protection, we also show how one can induce persistent localized bulk wave patterns by strategically placing defects in 2D lattice ATCs. These results lay the foundation for the practical implementation of autonomous electrical circuits with robust functionality in arbitrarily high dimensions.

Information transfer and storage in natural and man-made active systems, from sensory organs [1–3] to the internet, rely on the robust exchange of electrical signals between a large number of autonomous units that balance local energy uptake and dissipation [4, 5]. Recent advances in the understanding of photonic [6–8], acoustic [9] and mechanical [10–13] metamaterials have shown that topological protection [14–19] enables the stabilization and localization of signal propagation in passive and active [20, 21] dynamical systems that violate time-reversal and/or other symmetries. Important recent work has successfully applied these ideas to realize topoelectrical circuits [22] in the passive linear [23–28], passive nonlinear [29], and active linear regime [30]. De-

spite substantial progress in the development of topological nonlinear optics [31–35] and transmission lines [36–39], however, the generalization to active [40, 41] nonlinear circuits made from autonomously acting units still poses an unsolved challenge.

Exploiting a mathematical analogy with active Brownian particle systems [21], we develop and demonstrate general design principles for active topoelectrical circuits (ATCs) that achieve self-organized, self-sustained, topologically protected current patterns. The main building blocks of ATCs are nonlinear dissipative elements that exhibit an effectively negative resistance (NR) over a certain voltage range. NRs can be realized using van der Pol (vdP) circuits [42], tunnel diodes, unijunction transistors, solid-state thyristors [43], or operational amplifiers set as negative impedance converters through current inversion [30], and the design principles described below are applicable to all these systems. Indeed, we expect them to apply to an even broader class of nonlinear systems, as similar dynamics also describe electromagnetic resonators with Kerr-type nonlinearities [34, 44, 45].

Active electronic circuits with basic non-topological interactions have been studied previously as models of neuronal networks [42] and solitary signal transport [4, 5]. To leading order, the NR elements in an active circuit can be described [4, 5] by a Rayleigh-type resistance $R(V) = -(\alpha - 3\gamma V^2)$, where α and γ are positive parameters. A prototypical example is the vdP oscillator circuit with capacitance C and inductance L_{ii} , as shown in Fig. 1(a). When expressed in terms of the rescaled dimensionless voltage $\tilde{V}_i = x_i = \sqrt{3\gamma/\alpha} V_i$, the dynamics of an isolated vdP-unit i is governed by [46]

$$\ddot{x}_i - \varepsilon(1 - x_i^2)\dot{x}_i + x_i = 0, \quad (1)$$

where $\varepsilon = \alpha\sqrt{L/C}$, $t = \sqrt{LC}\hat{t}$, and $\dot{x}_i = dx_i/d\hat{t}$. Equation (1) is intimately related to that of a harmonically trapped active Brownian particle [47], with position coordinate y and velocity $u = \dot{y}$ described by the standard cubic friction model $\dot{u} = \varepsilon(1 - u^2/3)u - y$. Upon taking the time derivative and identifying $u = \dot{y} = x_i$, one recovers Eq. (1). It was shown recently [21] that suitably coupled mechanical chains of active Brownian particles can autonomously actuate topological modes. This in-

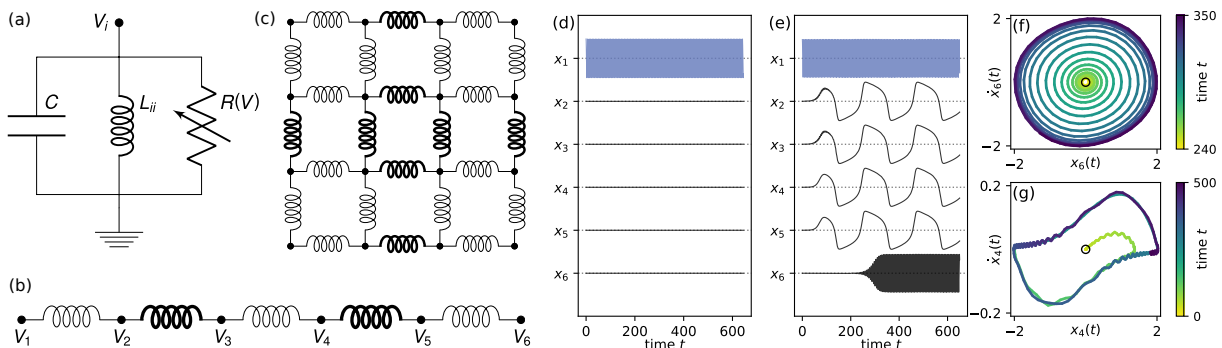


FIG. 1. Schematic and dynamics of active topoelectrical SSH circuits. (a) Circuit diagram of a basic vdP oscillator with capacitance C , inductance L_{ii} and nonlinear resistor $R(V)$. (b,c) 1D and 2D SSH circuits where each node is a vdP oscillator. Thick lines indicate strong coupling s and thin lines weak coupling $w \ll s$. (d) Oscillator dynamics in an undamped passive ($\varepsilon = 0$) 1D SSH circuit with 6 nodes. Applying a nonzero initial voltage at the first node, the oscillation remains exponentially localized on that edge. (e-g) Dynamics of a 1D ATC ($\varepsilon > 0$) for the same initial condition as in (d). The high-frequency topological edge mode is activated first and induces slow synchronized bulk oscillations, which eventually actuate the second topological mode at the opposite end. Phase portraits of the boundary (f) and bulk (g) nodes show the limit cycles of the fast and slow oscillations. The edge oscillators show approximately circular limit cycles typical of weak nonlinearity while the bulk dynamics is of strong relaxation type despite ε being small. Simulation parameters in (d-e): $g = 1$, $w = 0.003$, $s = g - w$ with $\varepsilon = 0$ in (d) and $\varepsilon = 0.1$ in (e-g). Initial conditions: $x_1(0) = 2$ and $\dot{x}_1(0) = \dot{x}_j(0) = \dot{x}_j(0) = 0$ for $j \geq 2$.

sight provides guidance for the design of ATCs.

To design an ATC with desired topological properties, we generalize Eq. (1) by introducing suitably chosen couplings between vdP units i and j through inductances L_{ij} ; see Fig. 1(b,c) for two examples. Assuming a lattice of vdP units and introducing the symmetric coupling matrix elements $\beta_{ij} = -L_0/L_{ij}$ for $i \neq j$, and $\beta_{ii} = L_0(1/L_{ii} + \sum_{k:k \neq i} 1/L_{ik})$, Eq. (1) generalizes to

$$\ddot{x}_i - \varepsilon (1 - x_i^2) \dot{x}_i + \sum_j \beta_{ij} x_j = 0, \quad (2)$$

where L_0 is the smallest inductance in the circuit (Supplementary Information).

Interpreting each individual vdP unit as a node in the network graph [Fig. 1(b,c)], the effective dimension d of the ATC can be tuned by increasing the number of couplings. In principle, arbitrary values $d \geq 1$ are realizable with large, densely connected networks [22]. For example, for d -dimensional cubic lattices, rows of the coupling matrix $\beta = (\beta_{ij})$ corresponding to bulk nodes will have $2d$ off-diagonal entries. Below, we will focus on the cases $d = 1$ [Fig. 1(b)] and $d = 2$ [Fig. 1(c)] to demonstrate the implementation and key properties of ATCs. Generally, through an appropriate choice of β , it is possible to realize a wide range of topological phases.

As a first realization of an ATC, we consider the coupling matrix of a one-dimensional (1D) Su-Schrieffer-Heeger (SSH) model. Originally introduced to describe polyacetylene [48], the SSH model is known to support topologically protected boundary modes in a variety of quantum [49] and classical [13, 21, 22] systems. The $n \times n$

SSH coupling matrix for the case of $n = 6$ unit vdPs reads

$$\beta = \begin{pmatrix} g & -w & 0 & 0 & 0 & 0 \\ -w & g & -s & 0 & 0 & 0 \\ 0 & -s & g & -w & 0 & 0 \\ 0 & 0 & -w & g & -s & 0 \\ 0 & 0 & 0 & -s & g & -w \\ 0 & 0 & 0 & 0 & -w & g \end{pmatrix}, \quad (3)$$

with the diagonal elements $\beta_{ii} = g > 0$ representing the electrical grounds. In our circuits, ground inductances L_{ii} are chosen such that $g = L_0(1/L_{ii} + \sum_{k:k \neq i} 1/L_{ik})$ for all i . Upon generalizing this coupling matrix by permitting non-uniform grounds g_i , one can achieve additional frequency control (Supplementary Information). The off-diagonal entries $w > 0$ and $s > w > 0$ encode the weak and strong couplings, respectively. Adding more units extends the matrix symmetrically along the diagonal. As in the original quantum SSH model, the strongly coupled nodes form ‘dimers’ which are connected to each other through weak bonds [thin lines in Fig. 1(b)].

To gain intuition about the dynamics of the 1D SSH circuit, it is instructive to first consider the undamped passive topoelectrical SSH circuit with $\varepsilon = 0$ and $s \gg w$. Then, Eqs. (2) and (3) reduce to a linear dynamical system that exhibits topologically protected, exponentially localized modes at both ends of the chain [49]. These edge modes have finite-frequency for $g > 0$ and become zero-modes as $g \rightarrow 0$. Their presence can be illustrated by considering an ideal passive ($\varepsilon = 0$) circuit [22] in the almost fully dimerized topological regime ($w \ll s$) with all nodes initially at rest, $x_i(t) = \dot{x}_i(t) = 0$ for $t < 0$. Upon initializing the chain by imposing a nonzero voltage value at the left edge, $x_1(0) > 0$, the boundary node

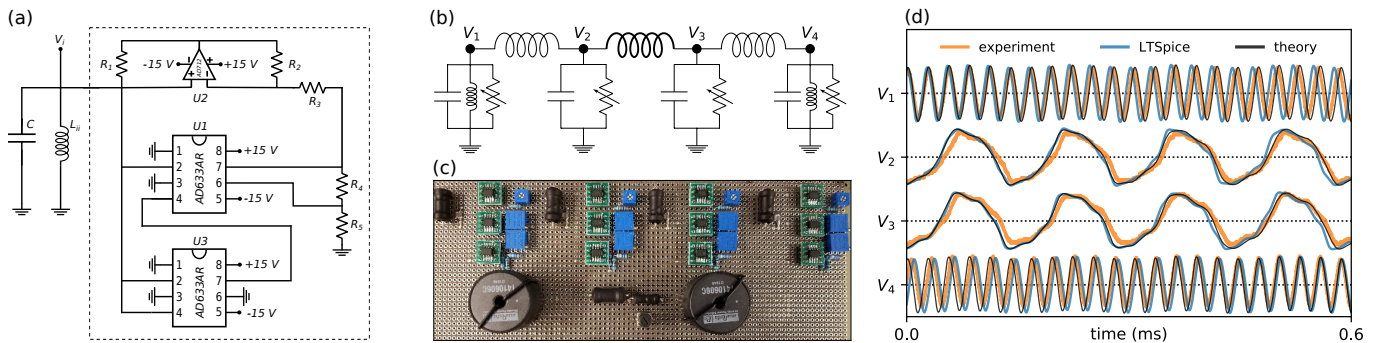


FIG. 2. Experimental realization of a 1D active topolelectric circuit with 4 nodes. (a) Implementation of a single active node using a Chua diode circuit (Supplementary Information). (b) Four-node active topolelectric circuit using $C = 42$ nF, $L_{12} = L_{34} = 10.5$ mH, $L_{23} = 525$ μ H. To obtain the classical SSH coupling matrix Eq. (3), no inductors were used for the bulk nodes, such that $L_{11} = L_{44} = 525$ μ H. The corresponding dimensionless parameters are $s = 1.0$, $w = 0.05$, $g = 1.05$, and $\varepsilon = 0.28$. (c) Experimental setup on circuit board. (d) Experimental data (orange lines), simulations of the full circuit using LTSpice (blue lines), and theoretical simulation using Eq. (2) match. Voltages V_1 – V_4 vary between ± 6 V, in-phase initial conditions were chosen on the two bulk oscillators.

will oscillate with a non-zero amplitude at frequency \sqrt{g} , while the amplitudes of the other nodes remain exponentially small [Fig. 1(d)]. In the next part, we will see that ATCs with $\varepsilon > 0$ exhibit fundamentally different behaviors that promise a broad range of novel applications.

Adding just a small amount of activity ($0 < \varepsilon \ll \sqrt{g}$) significantly alters the dynamics of the edge and bulk oscillators [Fig. 1(e–g)]. In the topological regime, characterized by $s \gg w$ and $g \geq s + w$, the boundary nodes are only weakly coupled to the bulk and behave similarly to isolated vdP oscillators. The active local energy input renders the rest state ($x_i = \dot{x}_i = 0$) unstable, forcing the boundary nodes to approach a stable limit cycle corresponding to an oscillation at frequency \sqrt{g} [Fig. 1(e,f)]. By contrast, bulk nodes are strongly coupled to one or more neighbors, resulting in a distinctly different bulk dynamics reminiscent of highly nonlinear relaxation oscillations [Fig. 1(e,g)]. For fully decoupled pairs of vdP oscillators, one expects stable phase-locked solutions with relative phase 0 or π [50, 51]. To obtain further analytical insight into the bulk dynamics, we linearize Eqs. (2) near the rest state. The resulting dynamical matrix has eigenvalues $\lambda_{k,\pm} = \frac{1}{2}(\varepsilon \pm \sqrt{\varepsilon^2 - 4\mu_k}) = \pm\sqrt{-\mu_k} + \mathcal{O}(\varepsilon)$, where μ_k are the eigenvalues of the coupling matrix β (Supplementary Information). In the fully dimerized limit ($w \rightarrow 0$), μ_k can be calculated explicitly and one finds two degenerate eigenstates at $\mu_k = g$, corresponding to the topologically protected edge modes, and $n - 2$ degenerate bulk modes at $\mu_k = g \pm s$ (Supplementary Information). The bulk eigenvectors are pairwise localized with components $(1, \pm 1)$ on one of the dimers, and zero everywhere else, corresponding to a low-energy in-phase oscillation ($\mu_k = g - s$) and a high-energy anti-phase ($\mu_k = g + s$) oscillation (Supplementary Information). This implies that the dimers' dynamics near the rest state is approximately decoupled and governed by the

eigenvalues $\sqrt{-g \mp s}$. If $g > s$, all modes are oscillatory, while for $g < s$, the anti-phase mode becomes unstable and is not physically realizable. Armed with these analytical insights, we proceed to numerically characterize the striking nonlinear effects that arise in ATCs. In the simulations, we can fix $g = 1$ without loss of generality, which is equivalent to dividing Eq. (2) by g and rescaling $t \rightarrow t/\sqrt{g}$, $\varepsilon \rightarrow \varepsilon/\sqrt{g}$, $s \rightarrow s/g$ and $w \rightarrow w/g$.

In contrast to passive ($\varepsilon = 0$) topolelectric circuits, which remain quiescent in the bulk when initiated at the edge [Fig. 1(d)], ATCs with $\varepsilon > 0$ exhibit complex self-organization and synchronization phenomena. To explain the underlying physical mechanisms, we consider the 1D SSH ATC from Fig. 1(b) with the same initial condition as for the passive circuit in Fig. 1(d). When one edge node of the ATC is initialized at time $t = 0$, it rapidly settles into a limit-cycle oscillation [Fig. 1(e,f)], as predicted above. As it gets activated, the edge mode imparts a weak external forcing on the neighboring strongly-coupled dimer. The combination of forcing and local energy input from the negative resistance drives the dimer into its low-energy state, characterized by a slow nonlinear in-phase oscillation of the dimer nodes with period $2\pi/\sqrt{g-s}$ [Fig. 1(e,g)]. The first bulk dimer then in turn activates the second dimer, and so on, resulting in a globally synchronized bulk state. The activation front eventually reaches the last node, where it triggers the second topological edge mode [Fig. 1(f)]. The final state of the chain is a robust attractor that is self-sustained and could be used for active solitary signal transmission.

As an experimental proof-of-concept demonstration of the above general concepts, we built a 1D 4-node ATC using a Chua diode circuit as the active element [Fig. 2(a,b)]. The measured time-series of the oscillator voltages exhibit the theoretically predicted topological edge modes and low-frequency bulk dynamics

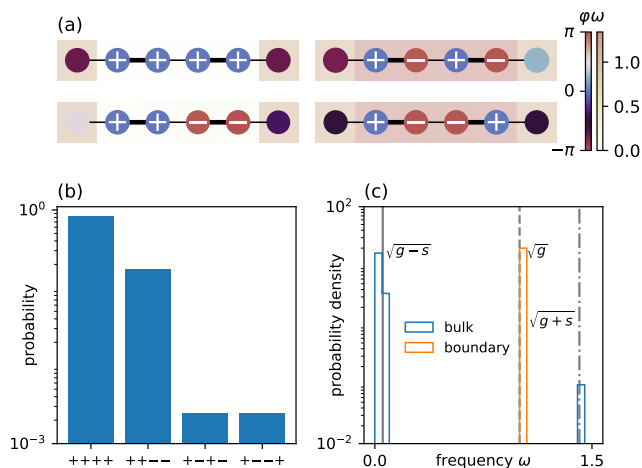


FIG. 3. Attractor statistics of a 1D ATC. (a) An active SSH circuit with $n = 6$ vdP nodes has four qualitatively distinct stable attractors. Circle size represents instantaneous absolute voltage $|x_i(t)|$, symbol color the phase φ and background color the time-averaged frequency $\omega = \langle \dot{\varphi} \rangle$ of the oscillators. Two low-energy attractors exhibit in-phase dynamics of the bulk dimer nodes, and two high-energy attractors show anti-phase dynamics on the bulk dimers. (b) Low-energy attractors are substantially more frequently realized when bulk nodes are initialized with uniformly random $x_i(0) \in [-4, 4]$ and $\dot{x}_i(0) \in [-0.4, 0.4]$. The two in-phase states are approached for $\approx 99.5\%$ of initial conditions. (c) Frequencies of nonlinear bulk oscillations cluster around $\sqrt{g} \pm s$ (solid/dash-dotted line), boundary oscillations around \sqrt{g} (dashed line), as predicted by linearized theory. Simulation parameters: $g = 1, w = 0.003, s = g - w$, and $\varepsilon = 0.1$. Histograms were computed from 50,000 trajectories, integrated up to $t = 1000$.

(Fig. 1). The quantitative agreement of the experiments with theory as well as explicit circuit simulations (Supplementary Information) confirms that Eq. (2) provides a predictive framework for ATCs – and that it is straightforward to realize topolectrical materials with off-the-shelf components. Indeed, the example in Fig. 2 is only one of many possible ATC implementations (Supplementary Information).

In practice, ATCs can be actuated with a wide range of initial conditions that can lead to different types of stable asymptotic behaviors (Fig. 3). To investigate the likelihood and characteristics of possible attractors, we used Eq. (2) to simulate an active SSH circuit with $n = 6$ nodes with non-zero initial conditions on the bulk. Since the edge node initial conditions become negligible in this case due to the weak edge-bulk coupling, we fixed zero-initial conditions at the edges. Thus, the topological edge modes are actuated by the bulk dynamics in these simulations. Examples of low-energy and high-energy attractors with slow and fast bulk dimer oscillations, obtained with binary initial conditions in the bulk, $x_i(0) = \pm 0.1$ and $\dot{x}_i(0) = 0$, are shown [Fig. 3(a)]. These attractors

can be classified in terms of the relative signs of the $n_b = n - 2 = 4$ bulk voltages x_i at a fixed time. Normalizing by the sign of the first bulk oscillator, we numerically find that there exist four different stable attractors corresponding to different possible combinations of in-phase and anti-phase dimer oscillations [Fig. 3(a)].

To estimate the likelihood of observing a specific attractor in experiments, we performed 50,000 simulations with randomly chosen bulk initial data. To explore a large neighborhood of the bulk limit cycle [Fig. 1(g)], initial conditions were sampled uniformly from the 8-dimensional domain $x_i(0) \in [-4, 4]$, $\dot{x}_i(0) \in [-0.4, 0.4]$. These simulations predict that, in practice, low-energy states with in-phase bulk dimers are much more likely than high-energy attractors with many anti-phase dimers [Fig. 3(b)]. Mixed in-phase/anti-phase dimer attractors are not observed for this parameter regime. Furthermore, even though the shape of the bulk limit cycles indicates a highly nonlinear relaxation dynamics [Fig. 1(g)], the numerically determined time-averaged frequencies $\langle \dot{\varphi} \rangle$, where $\varphi(t) = \arctan(\dot{x}(t)/x(t))$, agree remarkably well with the bulk oscillation frequencies $\sqrt{g} \pm s$ and boundary oscillation frequency \sqrt{g} predicted by the linearized theory above [Fig. 3(c)]. Based on these observations, one expects that low-energy attractors with in-phase bulk dimer dynamics will also be dominant in more complex ATCs, and that their bulk and edge frequencies can be estimated from spectra of the coupling matrix β in the weak coupling limit.

ATC implementations become particularly powerful in $d \geq 2$ dimensions. Different types of 2D SSH lattices can be constructed by stacking 1D SSH chains and connecting them using alternating strong and weak couplings (Fig. 4). This procedure allows the realization of two essentially different topological regimes: T1 – only the edges along one of the coordinate axes are in the topological coupling regime [Fig. 4(a,b)]; T2 – all the edges are in the topological coupling regime [Fig. 4(c-f)]. In the T1-regime, topologically protected modes exist along two opposite edges of a finite sample [Fig. 4(b), SI Movie 1], whereas in the T2-regime they exist on all four of the edges including the corners [23]. Because essential aspects of the dynamics are qualitatively similar for both cases, we focus our discussion on the T2-regime [Fig. 4(c), SI Movie 2]. In this case, one can distinguish three different groups of oscillators: corner oscillators that are only weakly coupled to their neighbors, strongly coupled vdP dimers along the edges that are similar to the 1D case, and quartets of strongly coupled vdP oscillators in the bulk. Each quartet is weakly coupled to its neighbors or the boundary. Analogous to the 1D case, the linear stability of the quartets can be analyzed independently in the weak-coupling limit $w \rightarrow 0$. Then, the lowest-frequency mode is an in-phase state $(1, 1; 1, 1)$ with period $2\pi/\sqrt{g - 2s}$ (Supplementary Information). Similar

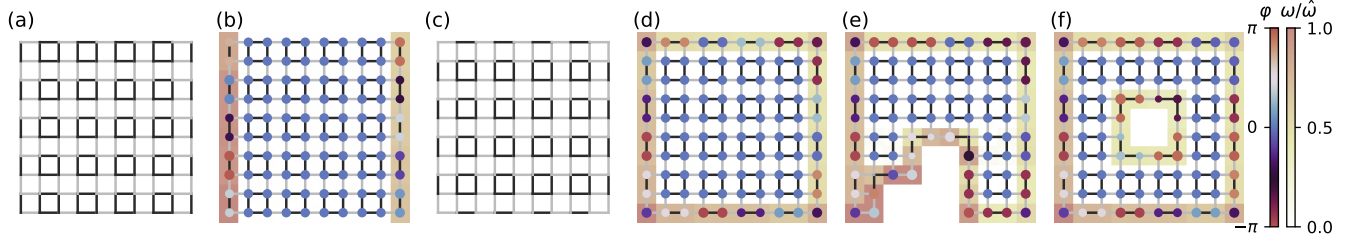


FIG. 4. Self-organized self-sustained nonlinear oscillations in 2D ATCs recapitulate topological boundary phenomena. (a) Connectivity of the 2D SSH grid in the topological T1-edge mode regime. Thick and thin lines indicate strong and weak couplings, respectively. (b) Snapshot of the vdP network dynamics on the grid (a), with nodes colored by the phase angle φ in the (x_i, \dot{x}_i) plane; background color shows time averaged node frequency $\omega = \langle \dot{\varphi} \rangle$ normalized by the maximum $\hat{\omega}$ over all oscillators. Even though the initial voltage was non-zero only on the bottom left corner node, the circuit autonomously actuates two topological edge oscillations with mean frequency $\hat{\omega}$, while the bulk synchronizes in-phase (SI Movie 1). (c) Connectivity of the 2D SSH grid in the topological T2-corner mode regime. (d) Snapshot of the vdP network dynamics on the grid (c), for the same corner-localized initial conditions as in (b). This circuit self-organizes into a stable active state in which edges and corners oscillate while the bulk synchronizes in-phase (SI Movie 2). (e,f) Snapshot of the vdP network dynamics on the grid (c) with edge (e) and bulk (f) defects. The vdP oscillator network remains polarized in the bulk, while active topological modes wrap around the defect (SI Movies 3,4). Simulation parameters: $\varepsilon = 0.1, g = 1, w = 5 \times 10^{-6}, s = g/2 - w$. Initial conditions: $x_1(0) = 2$ and $\dot{x}_1(0) = \dot{x}_j(0) = 0$ for $j \geq 2$.

to the 1D case, in the limit $(g - 2s) \rightarrow 0^+$, the bulk quartets collectively synchronize to the low-frequency in-phase state. However, the dimers on the boundary now oscillate at a frequency lower than that of the corner nodes, because $(g - s) \rightarrow s$ as $(g - 2s) \rightarrow 0^+$. This opens the intriguing possibility of using topological protected modes to precisely control active oscillations in 2D ATCs. In particular, by varying the ground inductances of each of the nodes one can control frequencies of each of the corner nodes, edge dimers, and bulk quartets (Supplementary Information).

Initializing the 2D active SSH circuits with a nonzero voltage at one of the corner nodes, one finds that essential qualitative features of the dynamics seen in 1D ATCs carry over to the 2D case. In particular, the boundary nodes belonging to topologically protected corner modes and edge modes become activated one after the other and settle down in their respective vdP limit cycles. Similarly, in the bulk, quartets of strongly coupled oscillators synchronize. Because the in-phase state is the lowest-energy attractor above the quiescent state, the bulk synchronizes in a global in-phase pattern [Fig. 4(b,d)]. Thus, in both 1D and 2D ATCs, topologically protected edge modes become activated via self-sustained oscillations, while the bulk dynamics is almost decoupled, leading to synchronization.

Crucially, this ATC self-organization principle remains valid in the presence of lattice defects, demonstrating that topological protection phenomena can survive in the nonlinear regime $\varepsilon > 0$ [Fig. 4(e,f)]. Introducing a boundary defect in a passive ($\varepsilon = 0$) 2D SSH grid by removing a few unit cells does not affect the localized nature of the edge state, which now wraps around

the defect due to topological protection from the linear coupling. Self-sustained oscillations in nonlinear active ($\varepsilon > 0$) circuits inherit this topological protection globally: in the presence of edge defects, all boundary nodes continue to oscillate at a high non-zero frequency while bulk quartets synchronize at low frequency [Fig. 4(e), SI Movie 3]. Similarly, bulk defects also lead to localized nonlinear edge oscillations [Fig. 4(f), SI Movie 4]. These results show that the SSH network topology can be used to precisely control the individual and collective behavior of coupled nonlinear oscillators. Furthermore, the above ideas can be extended to achieve control of active traveling wave patterns by means of non-topological defects. By strategically placing bulk defects, one can guide the self-organization of active wave patterns that can be ini-

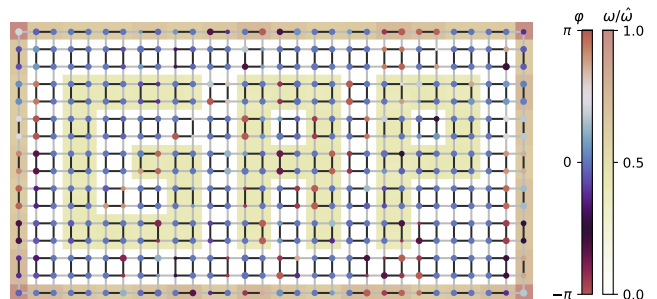


FIG. 5. Control of active traveling wave patterns through bulk defects. Activated in a single corner, the circuit self-organizes into a pre-programmed wave pattern (SI Movie 5). Simulation parameters: $\varepsilon = 0.5, g = 1, w = 5 \times 10^{-6}, s = g/2 - w$. Initial conditions: $x_1(0) = 2$ and $\dot{x}_1(0) = \dot{x}_j(0) = 0$ for $j \geq 2$.

tiated from a single corner node [Fig. 5, SI Movie 5].

In conclusion, active topoelectrical circuits promise a wide range of applications, from active wave guides to autonomous electronic circuits with topologically protected functionalities. The framework developed here can be integrated with recently developed methods for the inverse design of network-based metamaterial structures [52, 53], to optimize and tailor the node couplings and transmission properties. By designing the coupling matrix β such that the associated dynamical matrix possesses chiral [30] or other symmetries, it is possible to realize different topological phases by utilizing generic vDP-type nonlinearities. Another intriguing prospect is the possibility of creating and studying electronic metamaterials with effective dimensions $d > 3$ that appear to be difficult to access otherwise. Beyond man-made devices, the above results suggest that it would be interesting to explore whether active biological circuits may use topological coupling regimes to facilitate robust signal transport and information storage.

Acknowledgements. This work was supported by a James S. McDonnell Foundation Complex Systems Scholar Award (J.D.) and the MIT Solomon Buchsbaum Research Fund (J.D.). J.D. would like to thank the Isaac Newton Institute for Mathematical Sciences for support and hospitality during the program ‘The Mathematical Design of New Materials’ (supported by EPSRC grant EP/R014604/1) when work on this paper was undertaken. The work in Würzburg is funded by the Deutsche Forschungsgemeinschaft (DFG, German Research Foundation) through Project-ID 258499086 - SFB 1170 and through the Würzburg-Dresden Cluster of Excellence on Complexity and Topology in Quantum Matter – *ct.qmat* Project-ID 39085490 - EXC 2147.

-
- [1] R. FitzHugh, *Bull. Math. Biophysics* **17**, 257 (1955).
 [2] J. Nagumo, S. Arimoto, and S. Yoshizawa, *Proc. IRE* **50**, 2061 (1962).
 [3] E. Izhikevich, *Dynamical Systems in Neuroscience*, Computational neuroscience Dynamical systems in neuroscience (MIT Press, 2007).
 [4] V. A. Makarov, E. del Río, W. Ebeling, and M. G. Velarde, *Phys. Rev. E* **64**, 036601 (2001).
 [5] E. del Río, V. A. Makarov, M. G. Velarde, and W. Ebeling, *Phys. Rev. E* **67**, 056208 (2003).
 [6] S. Weimann, M. Kremer, Y. Plotnik, Y. Lumer, S. Nolte, K. G. Makris, M. Segev, M. C. Rechtsman, and A. Szameit, *Nat. Mater.* **16**, 433 (2017).
 [7] A. B. Khanikaev, S. Hossein Mousavi, W.-K. Tse, M. Kargarian, A. H. MacDonald, and G. Shvets, *Nat. Mater.* **12**, 233 (2013).
 [8] Y. Lumer, Y. Plotnik, M. C. Rechtsman, and M. Segev, *Phys. Rev. Lett.* **111**, 1 (2013).
 [9] Z. Yang, F. Gao, X. Shi, X. Lin, Z. Gao, Y. Chong, and B. Zhang, *Phys. Rev. Lett.* **114**, 114301 (2015).
 [10] C. Kane and T. Lubensky, *Nat. Phys.* **10**, 39 (2014).
 [11] S. D. Huber, *Nat. Phys.* **12**, 621 (2016).
 [12] L. M. Nash, D. Kleckner, A. Read, V. Vitelli, A. M. Turner, and W. T. Irvine, *Proc. Natl. Acad. Sci. U.S.A.* **112**, 14495 (2015).
 [13] B. G.-g. Chen, N. Upadhyaya, and V. Vitelli, *Proc. Natl. Acad. Sci. U.S.A.* **111**, 13004 (2014).
 [14] M. Z. Hasan and C. L. Kane, *Rev. Mod. Phys.* **82**, 3045 (2010).
 [15] B. A. Bernevig, T. L. Hughes, and S.-C. Zhang, *Science* **314**, 1757 (2006).
 [16] L. Fu, C. L. Kane, and E. J. Mele, *Phys. Rev. Lett.* **98**, 106803 (2007).
 [17] D. Hsieh, D. Qian, L. Wray, Y. Xia, Y. S. Hor, R. J. Cava, and M. Z. Hasan, *Nature* **452**, 970 (2008).
 [18] J. E. Moore and L. Balents, *Phys. Rev. B* **75**, 121306 (2007).
 [19] X. Qi and S.-C. Zhang, *Rev. Mod. Phys.* **83**, 1057 (2011).
 [20] A. Souslov, B. C. van Zuiden, D. Bartolo, and V. Vitelli, *Nat. Phys.* **13**, 1091 (2017).
 [21] F. G. Woodhouse, H. Ronellenfitsch, and J. Dunkel, *Phys. Rev. Lett.* **121**, 178001 (2018).
 [22] C. H. Lee, S. Imhof, C. Berger, F. Bayer, J. Brehm, L. W. Molenkamp, T. Kiessling, and R. Thomale, *Nat. Commun.* **1**, 39 (2018).
 [23] S. Imhof, C. Berger, F. Bayer, J. Brehm, L. W. Molenkamp, T. Kiessling, F. Schindler, C. H. Lee, M. Greiter, T. Neupert, and R. Thomale, *Nat. Phys.* **14**, 925 (2018).
 [24] T. Helbig, T. Hofmann, C. H. Lee, R. Thomale, S. Imhof, L. W. Molenkamp, and T. Kiessling, *Phys. Rev. B* **99**, 161114 (2019).
 [25] J. Ningyuan, C. Owens, A. Sommer, D. Schuster, and J. Simon, *Phys. Rev. X* **5**, 021031 (2015).
 [26] V. V. Albert, L. I. Glazman, and L. Jiang, *Phys. Rev. Lett.* **114**, 173902 (2015).
 [27] K. Luo, R. Yu, and H. Weng, *Research* **2018**, 6793752 (2018).
 [28] M. Ezawa, *Phys. Rev. B* **98**, 201402 (2018).
 [29] Y. Hadad, J. C. Soric, A. B. Khanikaev, and A. Alù, *Nat. Electron.* **1**, 178 (2018).
 [30] T. Hofmann, T. Helbig, C. H. Lee, M. Greiter, and R. Thomale, *Phys. Rev. Lett.* **122**, 247702 (2019).
 [31] X. Zhou, Y. Wang, D. Leykam, and Y. D. Chong, *New J. Phys.* **19**, 095002 (2017).
 [32] A. N. Poddubny and D. A. Smirnova, *Phys. Rev. A* **98**, 013827 (2018).
 [33] D. Leykam and Y. D. Chong, *Phys. Rev. Lett.* **117**, 143901 (2016).
 [34] D. Dobrykh, A. Yulin, A. Slobozhanyuk, A. Poddubny, and Y. S. Kivshar, *arXiv preprint arXiv:1805.03760* (2018).
 [35] S. Malzard and H. Schomerus, *New J. Phys.* **20**, 063044 (2018).
 [36] Y. Wang, L.-J. Lang, C. H. Lee, B. Zhang, and Y. Chong, *Nat. Commun.* **10**, 1102 (2019).
 [37] S. Sayed, S. Hong, and S. Datta, *Phys. Rev. Applied* **10**, 054044 (2018).
 [38] T. Jiang, M. Xiao, W.-J. Chen, L. Yang, Y. Fang, W. Y. Tam, and C. Chan, *Nat. Commun.* **10**, 434 (2019).
 [39] A. K. Iyer and G. V. Eleftheriades, *Appl. Phys. Lett.* **92**, 261106 (2008).
 [40] A. Forrow, F. G. Woodhouse, and J. Dunkel, *Phys. Rev. Lett.* **119**, 028102 (2017).
 [41] F. G. Woodhouse, A. Forrow, J. B. Fawcett, and

- J. Dunkel, *Proc. Natl. Acad. Sci. U.S.A.* **113**, 8200 (2016).
- [42] B. B. Johnson, S. V. Dhople, A. O. Hamadeh, and P. T. Krein, *IEEE Trans. Circuits Syst. I, Reg. Papers* **61**, 834 (2014).
- [43] I. Gottlieb, *Practical Oscillator Handbook* (Elsevier Science, 1997).
- [44] T. Morimoto and N. Nagaosa, *Sci. Adv.* **2**, e1501524 (2016).
- [45] T. Shi, H. J. Kimble, and J. I. Cirac, *Proc. Natl. Acad. Sci. U.S.A.* **114**, E8967 (2017).
- [46] J. J. Stoker, *Nonlinear vibrations in mechanical and electrical systems*, Vol. 2 (Interscience Publishers New York, 1950).
- [47] P. Romanczuk, M. Bär, W. Ebeling, B. Lindner, and L. Schimansky-Geier, *Eur. Phys. J. Special Topics* **202**, 1 (2012).
- [48] W. Su, J. Schrieffer, and A. J. Heeger, *Phys. Rev. Lett.* **42**, 1698 (1979).
- [49] J. K. Asbóth, L. Oroszlány, and A. Pályi, *A short course on topological insulators* (Springer).
- [50] D. Storti and R. Rand, *Int. J. Non-linear Mechan.* **17**, 143 (1982).
- [51] S. Wirkus and R. Rand, *Nonlinear Dyn.* **30**, 205 (2002).
- [52] A. Forrow, F. G. Woodhouse, and J. Dunkel, *Phys. Rev. X* **8**, 041043 (2018).
- [53] H. Ronellenfitsch, N. Stoop, A. Forrow, and J. Dunkel, *arXiv preprint arXiv:1802.07214* (2018).
- [54] G.-Q. Zhong, *IEEE Trans Circuits Syst-I* **41**, 934 (1994).

Supplementary Information

NONDIMENSIONALIZATION OF VARIABLES AND PARAMETERS

Given a lattice circuit, we state the equations of its voltage dynamics using Kirchoff's laws as follows:

$$C\ddot{V}_i - (\alpha - 3\gamma V_i^2)\dot{V}_i + \left(\frac{1}{L_{ii}} + \sum_{\substack{k \\ k \neq i}} \frac{1}{L_{ik}} \right) V_i - \sum_{\substack{j \\ j \neq i}} \frac{V_j}{L_{ij}} = 0, \quad (\text{S1})$$

where V_i is the voltage, C is the capacitance, L_{ii} is the ground inductance, and α and γ are the vdP parameters of the oscillator at node i , while L_{ij} are the coupling inductances between nodes i and j . The coupling inductances can be either of L_w or L_s where the subscripts w and s stand for weak and strong coupling respectively ($1/L_w < 1/L_s$). Note that for nodes i and k that are not connected, we have $1/L_{ik} = 0$.

We introduce a voltage scale $V_i = V_0 \hat{V}_i$, a time scale $t = \tau \hat{t}$, and we scale all the inductances by the smallest inductance, say L_0 , to get $L_{ij} = L_0 \hat{L}_{ij}$ for all i and j . For τ , we use the natural time scale of an oscillator such that $\tau = \sqrt{L_0 C}$, and the voltage scale is given by $V_0 = \sqrt{\alpha/(3\gamma)}$. The dimensionless dynamics is then given by Eq. (2) where $\hat{V}_i = x_i$, $\varepsilon = \alpha \sqrt{L_0/C}$, $\beta_{ij} = -L_0/L_{ij}$ for $i \neq j$, and $\beta_{ii} = L_0(1/L_{ii} + \sum_{\substack{k \\ k \neq i}} 1/L_{ik})$.

In Eq. (3), the weak and strong couplings are given by $w = L_0/L_w$ and $s = L_0/L_s$ respectively, while L_{ii} are chosen such that $g = L_0(1/L_{ii} + \sum_{\substack{k \\ k \neq i}} 1/L_{ik})$ for each i . To generalize the coupling matrix, we replace g by g_i to denote that each of them need not be equal to the other as we shall see in a later section (Frequency control).

EIGENVALUES OF THE COUPLING MATRIX

We now analyze the linear stability of the quiescent state ($x_i = 0$) of Eq. (2). We find for small deviations, by setting $\dot{x} = y$

$$\begin{pmatrix} \dot{x} \\ \dot{y} \end{pmatrix} = \begin{pmatrix} 0 & \mathbb{1} \\ -\beta & \varepsilon \mathbb{1} \end{pmatrix} \begin{pmatrix} x \\ y \end{pmatrix}. \quad (\text{S2})$$

The eigenvalue equation immediately gives us

$$\lambda^2 - \varepsilon \lambda = -\mu,$$

where μ is an eigenvalue of β and λ is an eigenvalue of the Jacobian. Thus, we obtain

$$\lambda = \frac{1}{2} \left(\varepsilon \pm \sqrt{\varepsilon^2 - 4\mu} \right),$$

to conclude that the most unstable mode occurs for μ minimal.

First, we compute the eigenvalues of the coupling matrix. We define

$$B_n = \begin{pmatrix} g & -w & 0 & \dots & 0 \\ -w & g & -s & & \\ \vdots & -s & \ddots & & \\ & & -w & g & -s \\ & & & -s & g & -w \\ 0 & \dots & & -w & g \end{pmatrix}, \quad (\text{S3})$$

$$C_{n-1} = \begin{pmatrix} g & -s & \dots & 0 \\ -s & \ddots & & \\ \vdots & -w & g & -s \\ & & -s & g & -w \\ 0 & \dots & -w & g \end{pmatrix}, \quad (\text{S4})$$

where B_n is an $n \times n$ matrix and C_{n-1} is an $(n-1) \times (n-1)$ matrix. Then the characteristic polynomial satisfies the recursion,

$$\chi(B_n, \mu) = (g - \mu)\chi(C_{n-1}, \mu) - w^2\chi(B_{n-2}, \mu), \quad (\text{S5a})$$

$$\chi(C_{n-1}, \mu) = (g - \mu)\chi(B_{n-2}, \mu) - s^2\chi(C_{n-3}, \mu), \quad (\text{S5b})$$

with initial conditions $\chi(B_2, \mu) = (g - \mu)^2 - w^2$ and $\chi(C_1, \mu) = g - \mu$. For simplicity we solve them in the fully dimerized limit, i.e., in the limiting case, $w = 0$, we find that

$$\chi(B_n, \mu) = (g - \mu)^2((g - \mu)^2 - s^2)^{n/2-1}, \quad (\text{S6})$$

with two modes corresponding to eigenvalue g (the topological edge modes), and rest of the modes corresponding to the symmetric eigenvalues $g \pm s$.

The eigenvectors x_i belonging to the eigenvalue g are $(1 \ 0 \ \dots \ 0)^\top$ and $(0 \ \dots \ 0 \ 1)^\top$ which are precisely the topological edge modes. Further, the eigenvectors corresponding to $g - s$ are the modes

$$\begin{aligned} & (0 \ 1 \ 1 \ 0 \ \dots \ 0)^\top, \\ & (0 \ 0 \ 0 \ 1 \ 1 \ 0 \ \dots \ 0)^\top, \\ & \vdots \\ & (0 \ \dots \ 0 \ 1 \ 1 \ 0)^\top, \end{aligned}$$

and those belonging to the eigenvalue $g + s$ are the modes

$$\begin{aligned} & (0 \ 1 \ -1 \ 0 \ \dots \ 0)^\top, \\ & (0 \ 0 \ 0 \ 1 \ -1 \ 0 \ \dots \ 0)^\top, \\ & \vdots \\ & (0 \ \dots \ 0 \ 1 \ -1 \ 0)^\top. \end{aligned}$$

The most unstable modes are those with the minimum eigenvalue, which are the degenerate ones belonging to $g - s$. Thus, this explains why the in-phase state is the probabilistically more preferred state. This concludes the analysis near the quiescent state.

We have shown that the quiescent state is unstable by finding the ‘most preferred’ eigenvectors if perturbed. We now analyze the behavior of the system away from the quiescent state. To simplify analysis, it is often useful to consider the system in the fully dimerized limit ($w = 0$). This amounts to analyzing sub-circuits made up of nodes that are only strongly coupled to each other. In essence, we are treating the ‘strong’ sub-circuit as independent to the rest of the network since it is connected to the rest of the network only through weak bonds (in other words, assume the weak bonds have zero strength).

FULLY DIMERIZED LIMIT

For the 1D SSH chain, in the fully dimerized limit, the system decouples into two isolated oscillators from the boundary nodes, and the rest-oscillator pairs from the bulk, called dimers. The dynamics of an isolated oscillator is given by

$$\ddot{x} - \varepsilon(1 - x^2)\dot{x} + gx = 0, \quad (\text{S7})$$

whose natural frequency is $\sqrt{g}/(2\pi)$. In the topological state, the edge nodes of the SSH chain will oscillate with this frequency. The internal dynamics of a dimer however are given by the equations

$$\ddot{x}_1 - \varepsilon(1 - x_1^2)\dot{x}_1 + gx_1 = sx_2, \quad (\text{S8a})$$

$$\ddot{x}_2 - \varepsilon(1 - x_2^2)\dot{x}_2 + gx_2 = sx_1, \quad (\text{S8b})$$

where x_1 and x_2 are the voltages of two adjacent nodes that are connected through a strong bond. It can be shown using eigenmode analysis, that the eigen-directions of the coupling matrix are $(1 \ 1)^\top$ (in-phase) and $(1 \ -1)^\top$ (anti-phase) with frequencies $\sqrt{g-s}/(2\pi)$ and $\sqrt{g+s}/(2\pi)$ respectively.

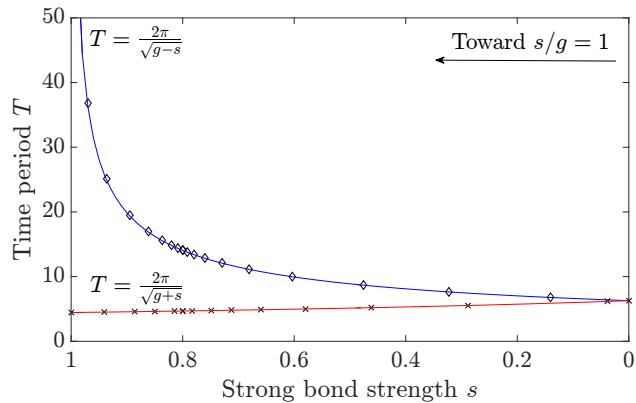


FIG. S1. Comparison of time periods of fully dimerized sub-circuits and bulk nodes in the SSH chain. Solid curves denote theoretical time period for in-phase and anti-phase modes of the dimer. Diamonds and crosses denote time periods of bulk nodes in the SSH chain at different values of s .

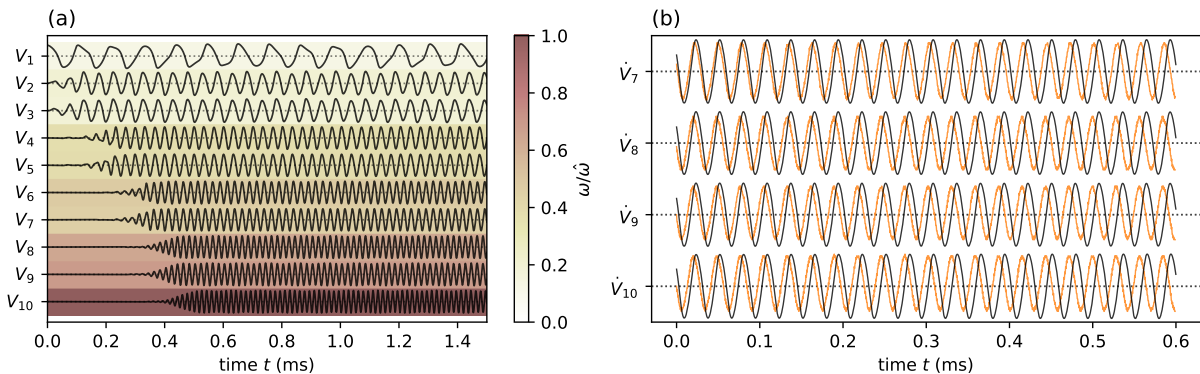


FIG. S2. (a) Theoretical time series of 10-node 1D SSH chain with localized frequency pattern. Darkening of background color denotes frequency increase along length of the chain. (b) Experimental and theoretical time series comparison for the low-energy in-phase attractor of 2D SSH sample in T2-corner mode regime. Since all ground inductances are equal, natural frequencies of all nodes are equal resulting in synchrony.

We see that the eigenmodes of the decoupled dimers and boundary nodes are consistent with the eigenmodes of the whole chain. In Fig. S1, there is a strong agreement between the time period of fully dimerized sub-circuits and that of the bulk nodes in the SSH chain. Thus, we have validation that taking the fully dimerized limit is in fact accurate and hence, can prove to be advantageous as shown. It also explains why in the topological regime, we have characteristically different behavior for the boundary (isolated nodes) and the bulk (dimers).

In the same way, we extend this theory for the 2D stacked SSH sample in which we analyze bulk quartets. The internal dynamics is given by a ring of van der Pol oscillators

$$\ddot{x}_1 - \varepsilon(1 - x_1^2)\dot{x}_1 + gx_1 = sx_2 + sx_4, \quad (\text{S9a})$$

$$\ddot{x}_2 - \varepsilon(1 - x_2^2)\dot{x}_2 + gx_2 = sx_3 + sx_1, \quad (\text{S9b})$$

$$\ddot{x}_3 - \varepsilon(1 - x_3^2)\dot{x}_3 + gx_3 = sx_4 + sx_2, \quad (\text{S9c})$$

$$\ddot{x}_4 - \varepsilon(1 - x_4^2)\dot{x}_4 + gx_4 = sx_1 + sx_3. \quad (\text{S9d})$$

Once again, it can be shown that the eigenmodes of the coupling matrix include the in-phase state (denoted by $(1 \ 1; 1 \ 1)$) and the anti-phase states (either $(1 \ -1; -1 \ 1)$ or $(1 \ 1; -1 \ -1)$ depending on which topological regime the network is in). It can be shown that the in-phase state is more stable than the anti-phase states, thereby favoring synchronization in the bulk. The natural frequencies of the bulk are calculated to be $\sqrt{g \pm s \pm \bar{s}}/(2\pi)$.

FREQUENCY CONTROL

We generalize the coupling matrix, Eq. (3) by replacing g by g_i to get

$$\beta = \begin{pmatrix} g_1 & -w & 0 & 0 & 0 & 0 \\ -w & g_2 & -s & 0 & 0 & 0 \\ 0 & -s & g_3 & -w & 0 & 0 \\ 0 & 0 & -w & g_4 & -s & 0 \\ 0 & 0 & 0 & -s & g_5 & -w \\ 0 & 0 & 0 & 0 & -w & g_6 \end{pmatrix}, \quad (\text{S10})$$

where $g_i = L_0(1/L_{ii} + \sum_{k \neq i} 1/L_{ik})$ such that L_{ii} can be chosen independently for each i . Since the frequencies of the dimers and quartets are proportional to $\sqrt{g_i \pm s}$ and $\sqrt{g_i \pm s \pm s}$ respectively, by varying L_{ii} appropriately, we can precisely control the frequency of each of the isolated nodes, dimers and quartets. We exploit this technique to construct two ATCs with specific frequency patterns.

In Fig. S2 (a), we construct a 1D SSH chain of 10 nodes where the ground inductances are chosen such that there is an increase in frequency by 10 kHz with each successive dimer/isolated node along the length of the chain. We obtain a precise, localized frequency pattern as can be seen via the background color darkening along the length of the chain.

In Fig. S2 (b), we consider a square 2D SSH sample in the T2-corner mode regime. Choosing the ground inductances of all nodes to be equal, say L , we get the same in-phase frequency for all of the isolated nodes, dimers and quartets. This can be seen via the following computations:

$$g_c = L_0 \left(\frac{1}{L} + \left(\frac{2}{L_w} \right) \right), \quad (\text{S11a})$$

$$g_e = L_0 \left(\frac{1}{L} + \left(\frac{2}{L_w} + \frac{1}{L_s} \right) \right), \quad (\text{S11b})$$

$$g_b = L_0 \left(\frac{1}{L} + \left(\frac{2}{L_w} + \frac{2}{L_s} \right) \right), \quad (\text{S11c})$$

$$s = \frac{L_0}{L_s}, \quad (\text{S11d})$$

$$g_c = g_e - s = g_b - 2s = L_0 \left(\frac{1}{L} + \frac{2}{L_w} \right), \quad (\text{S11e})$$

where the subscripts c , e and b stand for corner (isolated), edge (dimer) and bulk (quartet) respectively. This leads to a probabilistically favored synchronized state where the frequency of all nodes are equal. For the experiment, we make use of the same parameters used in Tab. II except that we include ground inductances for the bulk nodes this time. Once again, due to its topological nature, such states are robust against lattice defects.

ACTIVITY ONLY ON THE BOUNDARY

Global patterns can be realized in classical topological insulators by adding activity only to the boundary. This results in patching up of the localized topological modes giving rise to a global, robust state. Moreover, these states can be excited from the bulk as seen in the following simulations. We investigate by considering a 10×10 2D SSH sample in the T1-edge mode regime, T2-corner mode regime and the non-topological regime [Fig. S3]. Upon enabling activity only on the boundary, we excite the global topological state via an initial condition in the bulk. We observe that the samples in the topological regimes (a,b) display the same topological patterns with the added feature of exponential decay in amplitude as seen in classical passive systems. However, for the non-topological regime (c), we obtain oscillations only on nodes adjacent to the corners, indicating that global patterns in ATCs are not a consequence of adding activity alone; topology is also essential.

EXPERIMENTAL REALIZATION USING CHUA'S CIRCUIT

Our experimental realization of an active topoelectrical circuit implements a 4-node version of the circuit in Fig. 1(b) for nodes V_1 to V_4 . The individual circuit elements are off-the-shelf components from Digi-Key Electronics (Digi-Key

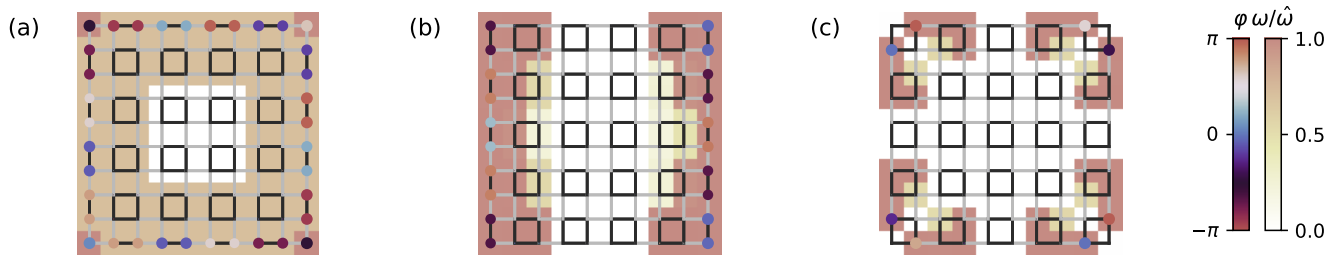


FIG. S3. Global topological states on 2D ATCs with activity only on the boundary (cf. Fig. 4). (a) Snapshot of the vdP network dynamics in the T2-corner mode regime, with nodes colored by the phase angle φ in the (x_i, \dot{x}_i) plane; background color shows time averaged node frequency $\omega = \langle \dot{\varphi} \rangle$ normalized by the maximum $\hat{\omega}$ over all oscillators. Even though the initial voltage was non-zero only on one node in the bulk, the circuit autonomously actuates the entire boundary with exponential decay in amplitude along the bulk. (b) Snapshot of the vdP network dynamics in the T1-edge mode regime. The circuit autonomously actuates two topological edge oscillations with exponential decay in amplitude along the bulk. (d) Snapshot of the vdP network dynamics in the non-topological regime. The circuit autonomously actuates nodes adjacent to the corners, but this state is neither topological nor global.

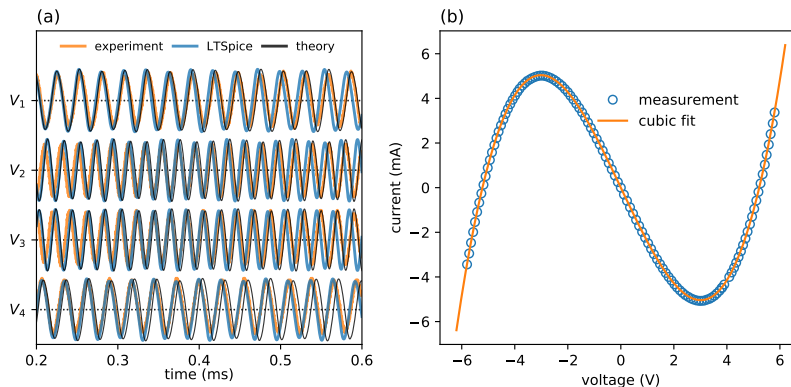


FIG. S4. (a) Experimental and theoretical time series comparison for the high-energy anti-phase attractor. The initial conditions on V_2 and V_3 had opposite signs. Orange lines correspond to experimental data, blue lines to LTSpice simulations and black lines to numerical simulations using Eq. (2) from the main paper. All voltages vary between ± 6 V. (b) Measured I - V characteristic curve of the Chua circuit. We applied voltages between -6 V and $+6$ V to the circuit and measured the current through the element, obtaining a cubic relationship. The fitted curve corresponds to the model $I(V) = -2.5 \text{ mS } V + 0.091 \text{ mS/V}^2 V^3$.

Electronics, Thief River Falls, MN, U.S.A.). For the active nonlinear resistance, we constructed a realization of Chua's diode [54] [Fig. 2(a)], which features a cubic current-voltage relationship. We measured the current through the Chua circuit when applying a voltage V_i and found almost perfectly cubic behavior [Fig. S4(b)]. We fitted the curve to a cubic polynomial and discarded the small constant and quadratic terms, which resulted in the simplified model $I(V) = -\alpha V + \gamma V^3$, which is also shown in Fig. S4(b). The parameters of all circuit elements are collected in Tables I and II.

The circuits were powered using two Extech 382260 80W switching DC power supplies (FLIR Commercial Systems, Nashuah, NH, U.S.A.), and measurements were taken using a Rigol DS 1054Z 4-channel digital oscilloscope (Rigol Technologies U.S.A., Beaverton, OR, U.S.A.).

Fig. S4 (a) shows an alternate dynamical attractor which is the high-energy bulk oscillation obtained using anti-phase initial conditions. This state is achieved using the same experimental setup in Fig. 2.

TUNING WAVE-LIKE PATTERNS USING DEFECTS

Active traveling wave patterns can be induced in the bulk of an ATC by strategically placing bulk defects. By replacing one of the strong bonds by a weak bond in the desired bulk quartets, it is possible to construct arbitrary

Dimensional parameter	Value	Nondimensional parameter	Value
C	42 nF	g	1.05
L_e	525 μ H	w	0.05
L_b	Nil	s	1.0
L_w	10.5 mH	ε	0.28
L_s	525 μ H		
α	2.5 mS	Scaling factor	Value
γ	0.091 mS/V ²	V_0	3.03 V
R_1	2 k Ω	τ	4.7 μ s
R_2	2 k Ω	L_0	525 μ H
R_3	400 Ω		
R_4	3010 Ω		
R_5	7900 Ω		

TABLE I. Realistic parameter values for the topological regime for a 1D SSH chain. L_w and L_s denote the inductances in the weak and strong couplings respectively while L_e and L_b denote the ground inductances of the edge and bulk nodes. Note that for the bulk nodes, we do not use ground inductances.

Component/Parameter	Node 1	Node 2	Node 3	Node 4
α	2.496 mS	2.494 mS	2.500 mS	2.500 mS
γ	0.09094 mS/V ²	0.09112 mS/V ²	0.09200 mS/V ²	0.09092 mS/V ²
L_{ii}	485.6 μ H	Nil	Nil	486.0 μ H
L_{ii} ESR	0.821 Ω	Nil	Nil	0.810 Ω
C	41.99 nF	41.63 nF	42.07 nF	42.06 nF
C ESR	0.459 Ω	0.620 Ω	0.704 Ω	0.760 Ω
L_w	10.5020 mH		10.5060 mH	
L_w ESR	2.520 Ω		2.528 Ω	
L_s	512.0 μ H			
L_s ESR	0.940 Ω			

TABLE II. Component values used for experiments in Figs. 2 and S4. ESR stands for equivalent series resistance, referring to the parasitic resistance present in practical, non-ideal inductors and capacitors. For the values listed, ESR was measured at an AC frequency of 1 kHz.

directional patterns. For instance, a circuit may be constructed to display text or images [Fig. 5]. The individual constituent segments of this active pattern interact with each other to produce traveling wave-like dynamics.

ALTERNATIVE EXPERIMENTAL SETUP

Here we discuss an alternative way to experimentally implement the cubic nonlinearity analyzed in the main paper, and present LTSpice simulations of a 6-node active topoelectric chain using this model.

Parameter scaling

For this realization, the scales for capacitance and inductance are set to as $C_0 = 100$ nF and $L_0 = 1.5$ μ H. It follows that the system's frequency scale is $\omega_0 = \frac{1}{\tau} = \frac{1}{\sqrt{L_0 C_0}} = 2\pi \cdot 411$ kHz and that of resistance $R_0 = \frac{1}{\varepsilon} = \sqrt{\frac{L_0}{C_0}} = 3.87$ Ω . These values are chosen to accommodate for what inductors and capacitors are easily available and to respect the limitations of the following non-linear resistor implementation in terms of operating frequency and output current.

Implementation of the non-linear resistor

The vdP oscillator requires a non-linear resistor element that behaves according to $R(V)^{-1} = -(\alpha - 3\gamma V^2)$. Ref. [54] suggests such an implementation using a negative impedance converter to create the negative conductivity at low applied voltages in parallel to two diodes acting as large positive-valued conductivities at higher voltages. The exact configuration used in our simulations is displayed in figure S5a. The diodes used are type 1N5817 Schottky

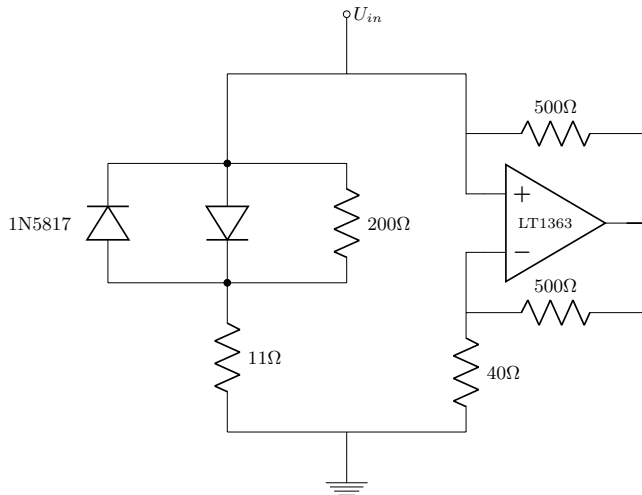
diodes, chosen for their low forward voltage drop to keep the oscillator chain's operating voltage low. This reduces the required current rating for other components. Figure S5b shows the non-linear resistor's DC current response and a third order polynomial fit to the region ± 200 mV. As can be seen, the element matches the U^3 function closely up to about ± 250 mV. Beyond that, the current response is smaller than the ideal behavior. From the fit curve, the parameters values of the non-linear resistor are determined as $\alpha = 0.0756$ and $\gamma = 0.408 \text{ V}^{-2}$. In order to test its usable frequency bandwidth, the circuit's response to an AC voltage of 500 mV is simulated at various frequencies. Figure S6 shows the current response within one period plotted over the input voltage. At 10 kHz, the curve approximately matches the DC behavior. Towards higher frequencies however, starting in the 100 kHz range, the current shows an increasing phase shift to the input voltage, visible as a loop forming in the current-voltage-plot. In simulations of the entire oscillator chain, this behavior has shown to cause problems at frequencies beyond 1 MHz, restricting the choice of other circuit parameters to the sub-megahertz range in $\frac{\omega_0}{2\pi}$.

Simulating the chain

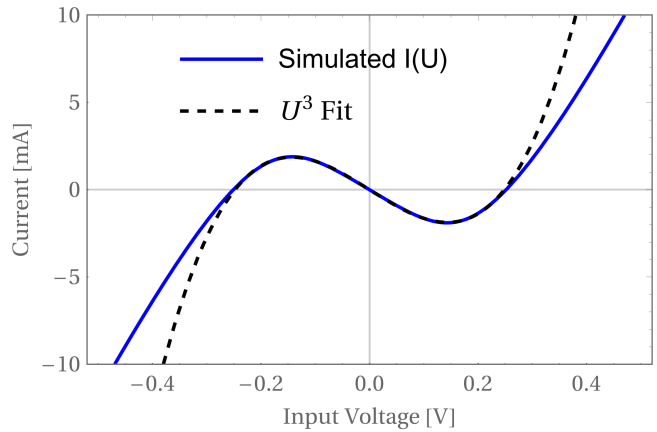
Figure S7 shows the chain's circuit diagram. Each node of the vdP oscillator chain is connected to ground via one of the non-linear resistors and a $100 \mu\text{F}$ capacitor in parallel, and to its neighboring nodes alternately by a $470 \mu\text{H}$ and a $1.5 \mu\text{H}$ inductor. The corresponding nondimensionalized parameter values are $g = 1$, $w = 0.00318$, $s = 1 - w$. The circuit has six nodes in total. To excite the left edge mode, a current I_{in} can be fed into the first node.

Idealized case

A simulation of the idealized case, neglecting parasitic resistances, was performed using LTSpice. The circuit is initialized with all currents and voltages set to zero. The left edge mode at node 1 is briefly excited using a current source at resonance frequency to reach the steady-state oscillation. Figure S8a shows the result of the transient simulation of all six nodes. In agreement with the numerical results of the main paper, the edges show a high-frequency oscillatory behavior, at about 410 kHz, while the bulk shows a slower oscillatory pattern at frequency 25 kHz. Amplitudes are typically about 300 mV. For the bulk nodes, an initial excitation at 575 kHz is observed that diminishes as the slow non-linear limit cycles settle. These oscillations are not visible in Fig. 1 of the main paper. This may be caused by the different means of initializing the system, where Fig. 1 uses nonzero initial conditions for x and \dot{x} while here, we briefly resonantly excite node 1 by an input current.



(a) Circuit diagram of the alternative non-linear resistor for the vdP oscillator.



(b) DC sweep of the non-linear resistor's input current and polynomial fit of third order. The resulting fit function is $I = - (0.01954 \Omega^{-1} \cdot U - 0.3169 \Omega^{-1} \text{V}^{-2} \cdot U^3)$, corresponding to parameter values $\alpha = 0.0756$ and $\gamma = 0.408 \text{ V}^{-2}$.

FIG. S5. Alternative circuit implementing a cubic nonlinearity.

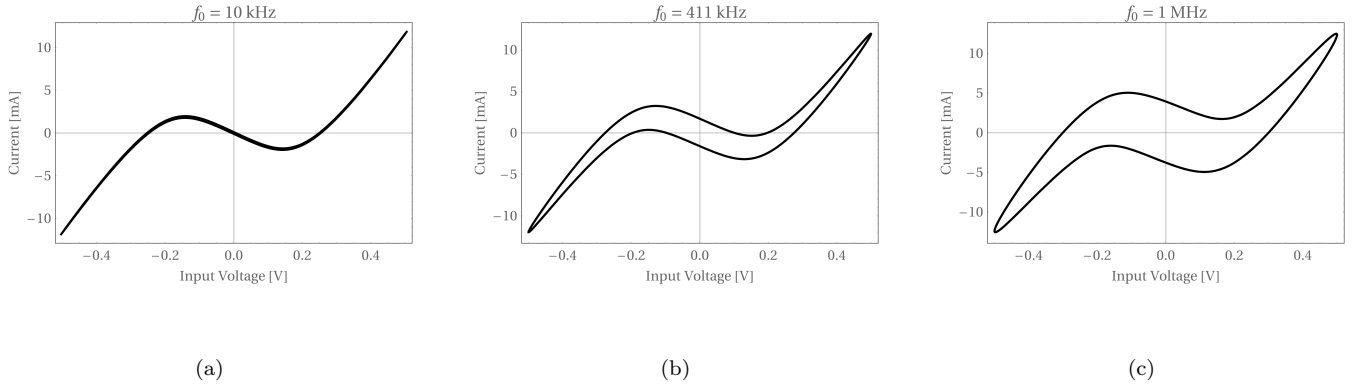


FIG. S6. Current over voltage plot of the non-linear resistor's response to an AC voltage of 500 mV at different frequencies.

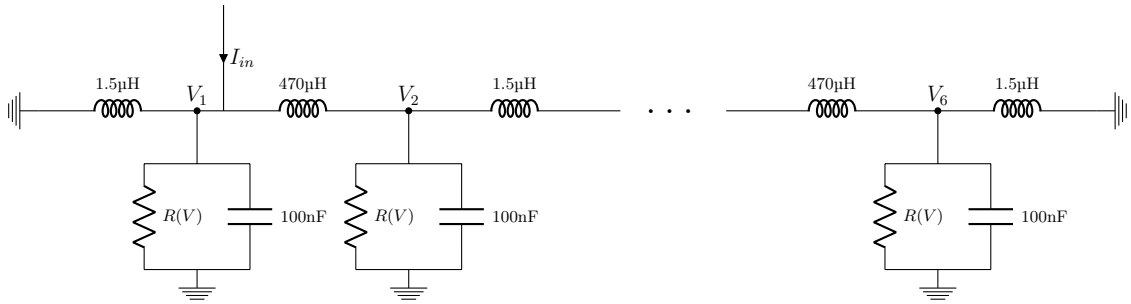


FIG. S7. Circuit diagram of the oscillator chain.

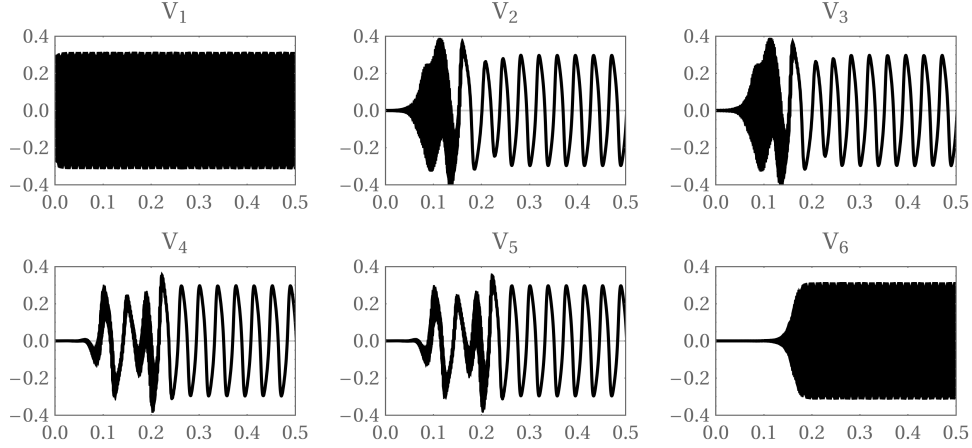
Including parasitic resistances

In order to obtain a more realistic simulation of the circuit, parasitic serial resistances are added to the inductors and capacitors of the circuit and disorder in the form of a 10% tolerance random deviation is applied to all passive elements. The chosen serial resistances for the inductors are $24.2\ \Omega$, corresponding to a Q-Factor of $Q @ 411\text{kHz} = 50$ for $470\ \mu\text{H}$ one and $110\ \text{m}\Omega$, corresponding to $Q @ 411\text{kHz} = 35$ for the $1.5\ \mu\text{H}$ one. The capacitors at node 1 and 6 have a serial resistance of $50\ \text{m}\Omega$, those in the bulk $5\ \Omega$. The different choice of the capacitor's serial resistance is an attempt to reflect the frequency dependent resistance of capacitors and also demonstrates that the bulk cycles are rather insensitive to a large serial resistance in the node's capacitor. Figure S9 shows the results of the transient simulation. Qualitatively, the circuit's behavior does not change by much. The only obvious difference is that the bulk nodes no longer show initial high frequency oscillations that now presumably are strongly damped by the parasitic resistances. Overall, the circuit's voltage amplitudes have somewhat diminished with the edge nodes at about 175mV and the bulk nodes at around 230 mV. The frequency of the edge modes is slightly lower compared to the ideal case at about 400 kHz. Much more significant is the change in the bulk cycle frequency that is more than halved to about 11 kHz. Re-running the simulation for various different parameter values shows that both the inductors and the capacitor's parasitic resistances contribute significantly to this effect, with the inductor's serial resistance having the comparatively larger influence on the bulk cycle's frequency. Figures S9b and S9c again show \dot{V} over V of the circuit's fourth and sixth node. As for the ideal case, that of node four resembles a non-linear limit cycle and that of node six a linear mode. Compared to the ideal case, the amplitude at node six grows slower, caused by the additional damping of the parasitic resistances.

When further increasing parasitic resistances, several modes of failure can occur that are listed in Table III. The main concerns are the edge modes potentially being damped or the bulk oscillations stalling for large serial resistances. To a certain degree, this can be compensated by adjusting the non-linear resistor element for a stronger driving. Larger disorder has relatively little effect on the qualitative behavior of the circuit, unless it locally induces a failure if some inductor or capacitor's Q is too low.

Element	Threshold	Effect
R_S of 470 μH inductor	$> 30 \Omega$	Bulk voltages stop oscillating, stall at constant value
R_S of 1.5 μH inductor	$> 200 \text{ m}\Omega$	Edge modes are damped
R_S of capacitors at edge	$> 150 \text{ m}\Omega$	Edge modes are damped
R_S of capacitors in bulk	$> 50 \Omega$	No failure but bulk cycles take on trapezoid shape

TABLE III. Observed modes of failure induced by large parasitic resistances.



(a) Transient voltage simulation of all six nodes for the ideal circuit. The horizontal axis is time in ms, vertical the voltage in V.

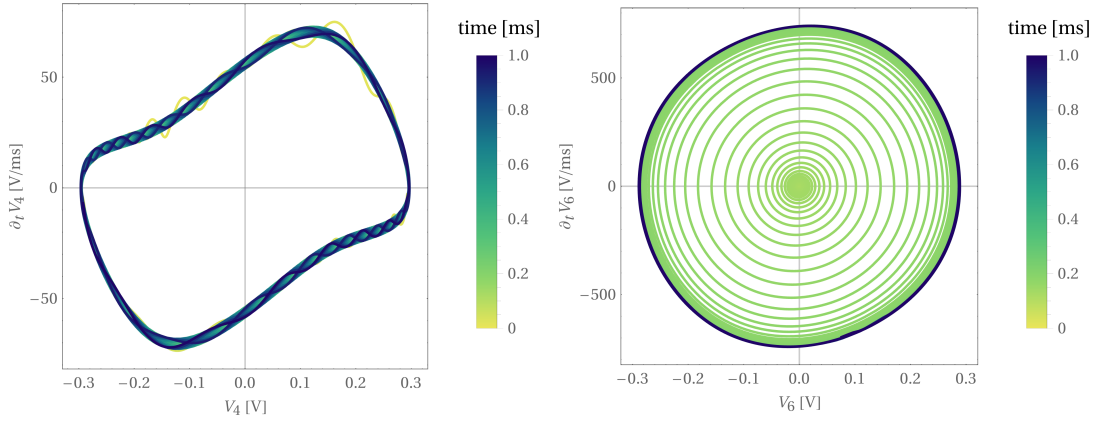
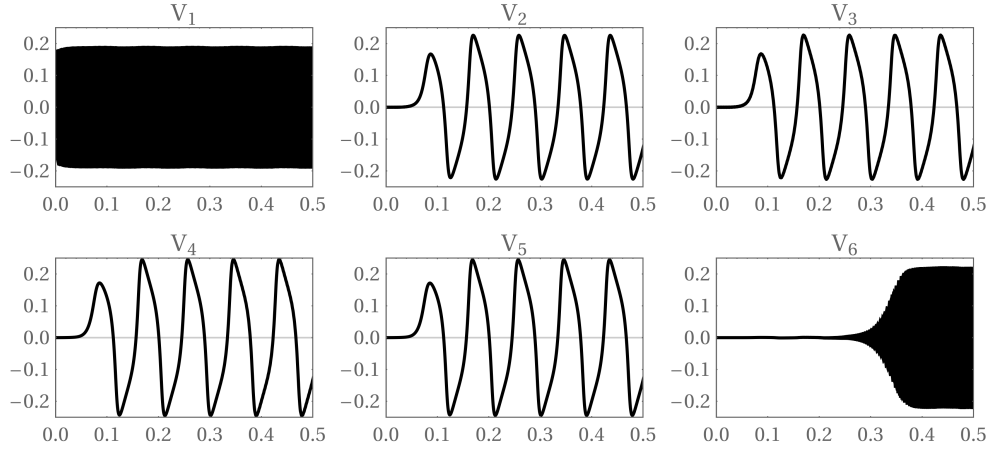
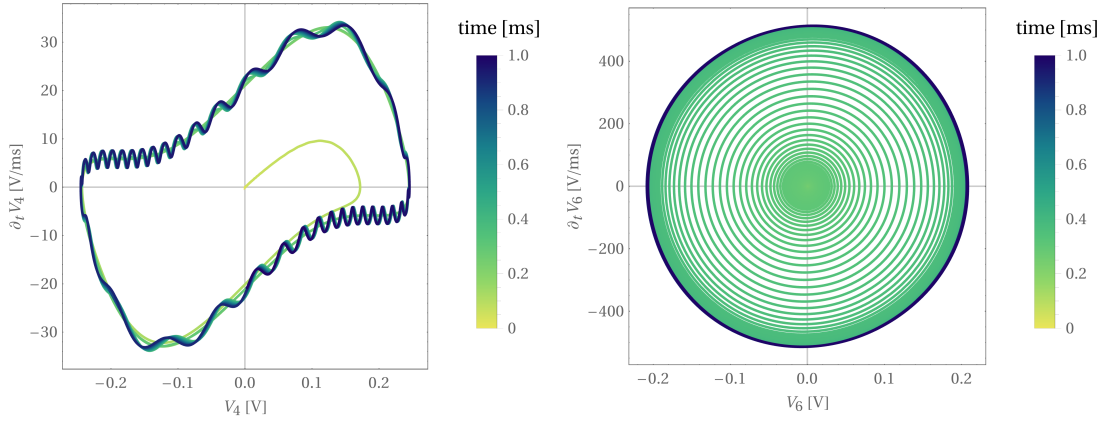
(b) (V, \dot{V}) plot of node 4 for the ideal circuit. The first 0.25 ms are cropped out due to the overlaid high frequency oscillation as seen in S8a. The non-circular shape implies that it is a strongly non-linear limit cycle.(c) (V, \dot{V}) plot of node 6 for the ideal circuit. The circular shape is close to that of a linear oscillation.

FIG. S8. Simulation results for the idealized alternative active topoelectric circuit using LTSpice.



(a) Transient voltage simulation of all six nodes for the circuit with parasitic resistances. The horizontal axis is time in ms, vertical the voltage in V.



(b) (V, \dot{V}) plot of node 4 for the realistic circuit. The first 0.25 ms are cropped out due to the overlaid high frequency oscillation as seen in [S8a](#). The non-circular shape implies that it is a strongly non-linear limit cycle.

(c) (V, \dot{V}) plot of node 6 for the realistic circuit. The circular shape is close to that of a linear oscillation.

FIG. S9. Simulation results for the alternative active topolectric circuit using LTSpice, including parasitic resistances.